An Active Damping Control Strategy to Enhance the Stability of High Voltage DC Power Supply System for More Electric Aircraft

Yiming Yao, Zhuoran Zhang, *Senior Member, IEEE*, Yankun Wang, *Graduate Student Member, IEEE*, Yiwei Yang, Heng Shi, and Jincai Li

***Abstract*—With the increasing integration of motors and power electronic converters into the electric power system (EPS) of the more electric aircraft (MEA), the proportion of constant power load (CPL) continues to rise. This poses significant challenges to the stability of onboard EPS. In this article, an active damping control strategy is proposed for the high-voltage dc power supply system utilizing a wound rotor synchronous generator. First, the output impedance of the system is derived using small-signal modeling. Based on the impedance criterion, the impacts of CPL power and control parameters on system stability are analyzed. Subsequently, the effects of various active damping positions and configurations are analyzed and compared, with the virtual resistance-capacitance series ultimately selected as the optimal active damping scheme. Finally, the implementation of the active damping control strategy is derived and refined. Experimental results confirm the effectiveness of the proposed method in enhancing system stability.**

***Index Terms*—Active damping control strategy, constant power load (CPL), impedance model, more electric aircraft (MEA), stability, wound rotor synchronous generator (WRSG).**

I. Introduction

THE rapid growth of the aviation industry has raised increasing concerns over its pollutant emissions. In response, the concept of the more electric aircraft (MEA) was introduced, which integrates secondary energy sources such as hydraulic, pneumatic, and mechanical energy into electrical energy [1], [2], [3]. This unification simplifies the aircraft's energy system structure and enhances both fuel efficiency and overall economic performance. Additionally, it reduces the emissions and noise, and represents the future direction of aviation development [3], [4], [5].

Among electric power supply systems for aircraft electrical power system (EPS), the high-voltage dc (HVDC) system is preferred over the alternating current (ac) system due to its advantages in size, weight, operational efficiency, reliability, and load compatibility [5], [6], [7]. Additionally, the HVDC system is more easily integrated with energy storage devices, thereby enhancing the power quality of EPS [6].

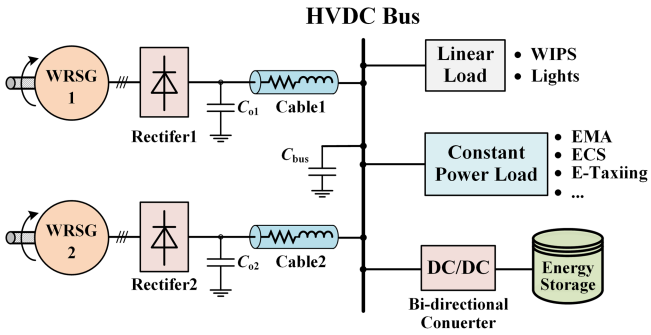

Fig. 1. Typical EPS architecture of a MEA.

Compared to traditional aircraft, the use of electric motors and power electronic converters in MEA has significantly increased [8], [9]. Fig. 1 illustrates a typical EPS architecture for a MEA, including the electro-mechanical actuator (EMA), electric environment control system, E-taxiing devices, and other components. Each component operates using either a speed closed-loop or position closed-loop control strategy, and can be classified as the constant power load (CPL) [10]. The negative impedance characteristic at the CPL input port can cause the system to deviate from its normal operating point, potentially leading to instability or even system failure. Therefore, ensuring the stability of the HVDC system is a critical consideration for MEA.

HVDC systems are typically regarded as cascaded systems. Therefore, the impedance models of the source and load subsystems in the EPS are commonly developed using small-signal analysis [11], [12], [13], [14], [15], [16]. This allows for system stability analysis through impedance criteria, which examine the interaction between the source output impedance and the load input impedance.

In [12], a small-signal model of a wound rotor synchronous generator (WRSG) based HVDC system is developed, and the effects of control bandwidth and filter capacitor size on the output impedance are analyzed. However, only the system under single-voltage loop control is modeled, and the effect of CPL on

Received 9 October 2024; revised 6 February 2025 and 1 March 2025; accepted 20 March 2025. Date of publication 24 March 2025; date of current version 26 May 2025. Recommended for publication by Associate Editor A. J. Marques Cardoso. *(Corresponding author: Zhuoran Zhang.)*

The authors are with the Jiangsu Key Laboratory of New Energy Generation and Power Conversion, Nanjing University of Aeronautics and Astronautics, Nanjing 211106, China (e-mail: hemec_yym@nuaa.edu.cn; apsc-zzr@nuaa.edu.cn; yankunwang@nuaa.edu.cn; ywyang@nuaa.edu.cn; sh@nuaa.edu.cn; cae_vsvf@nuaa.edu.cn).

Color versions of one or more figures in this article are available at https://doi.org/10.1109/TPEL.2025.3554267.

Digital Object Identifier 10.1109/TPEL.2025.3554267

the system is not considered. The impedance model of a permanent magnet synchronous generator (PMSG) based HVDC system is derived in [11], where the impact of CPL on system stability is analyzed [13]. This work is further extended to a multisource parallel system, where the influence of the number of parallel generators, load-sharing ratio, and droop control coefficient on system stability is evaluated [14], [15], [16].

Based on stability analysis, system stability can be improved by reshaping the impedance of either the source or load subsystem. Methods for doing so are classified into active damping and passive damping. Passive damping involves adding damping components or devices to the system, which increases its size and weight. Active damping is generally preferred, as it enhances stability by injecting linear or nonlinear compensation signals into the control strategy, thus avoiding the need to add components.

Specifically, active damping methods can be broadly classified into two categories: 1) source-side compensation and 2) load-side compensation [17], [18], [19]. While load-side active damping schemes can enhance system stability, they may adversely affect the load's operational performance [17]. Moreover, in systems with multiple CPL, the integrated impedance characteristics of all CPL must be comprehensively analyzed, complicating the parametric design process.

In contrast, source-side compensation is widely preferred due to its superior scalability, flexibility, and design simplicity, and has been widely studied in the fields of renewable energy, data centers, electric vehicles, and rail transportation [19]. In [20], an active damping strategy based on virtual resistance in series is proposed to solve the interaction stability problem between *LC* input filters and CPL in dc microgrids. And the virtual resistor is designed to be effective around the resonant frequency of the *LC* filter, thus reducing its output impedance. Based on this, a virtual inductance is connected in parallel to the virtual resistance to form an *RL* branch in [21], which solves the issue of poor voltage regulation caused by a single virtual resistance.

Parallel virtual impedance is also an effective approach. In [22], an optimized parallel virtual resistance based active damping control strategy is proposed for dc microgrid, the resistance value to enable stable operation in the whole power range is given. A virtual *R*-*C* connected in parallel with the bus capacitor is proposed in [17] and [18], and the effect of control strategies on dynamic performance is analyzed.

For the HVDC EPS in MEA, a voltage sag pass-through control and point of load control method in [13] are proposed to reduce the output impedance of the source subsystem and enhance system stability. A load current compensation method is introduced in [23], with its effectiveness analyzed at different locations, such as the voltage loop and current loop. Experimental results verify the method's effectiveness. However, these methods primarily target PMSG-based HVDC systems.

As the most widely utilized generator type in aircraft EPS, the existing literature mainly focuses on enhancing the dynamic performance of WRSG. In [24], load current and WRSG speed are incorporated as feedforward compensation into the conventional dual closed-loop control of voltage and field current, forming a multiloop proportional integral (PI) control strategy to improve dynamic response. In [25], fuzzy PI control is employed to enhance the dynamic performance of WRSGs under a wide speed range. Furthermore, advanced control strategies, such as dual internal model control [26], backstepping control [27], and robust control [28], have been progressively integrated into WRSG control frameworks. Nevertheless, research on stability enhancement under CPL operation remains relatively scarce.

For dc–dc converters or PMSG, the dual closed-loop control inherently includes terms related to the output current (*dq*-axis current or inductor current). Consequently, it is sufficient to feedforward the product of the load current and virtual impedance or the output voltage and virtual conductance into the control loop. However, in the case of the WRSG, only the field current is correlated in the closed-loop control, thereby introducing a challenge to the design and implementation of the active damping strategies. In addition, the WRSG exhibits pronounced nonlinearity, making it essential to ensure the stability of CPL operation under full-load conditions. Therefore, this article proposes an active damping control strategy to enhance the stability of an HVDC power supply system based on a single WRSG. The main contributions of the article can be highlighted as follows.

1) A detailed small-signal impedance model under double-closed-loop control is derived, based on the characteristics of the WRSG. The impact of CPL on system stability is thoroughly analyzed, and the limitations of conventional PI control are discussed.
2) The effects of virtual impedance location and configuration on stability enhancement are systematically investigated. Both transient and steady-state effects are analyzed, leading to the proposal of an active damping control strategy utilizing a virtual resistor-capacitor series configuration.
3) Based on the closed-loop control of the WRSG, the relationship between the output current and the field current is derived and extended to full-load conditions, accounting for the strong nonlinearity of the WRSG. Furthermore, the stability boundaries of the system are summarized, and parameter selection methods are provided.

The rest of this article is organized as follows. Section II presents the impedance modeling of the WRSG. The transfer function of the output impedance is derived and parameterized. In Section III, stability is analyzed and the limitations of conventional PI control are discussed. Then an active damping control strategy for the WRSG is proposed. The positions and configurations of the active damping are analyzed, the active damping function is derived and simplified in combination with the actual control, and a parameter design method is also given. To verify the effectiveness of the proposed control strategy, experimental verification is presented in Section IV. Finally, Section V concludes this article.

II. Impedance Modeling of the WRSG-Based HVDC Power Supply System

In this section, a single-channel WRSG-based HVDC power supply system is analyzed and its structural diagram is shown in Fig. 1.

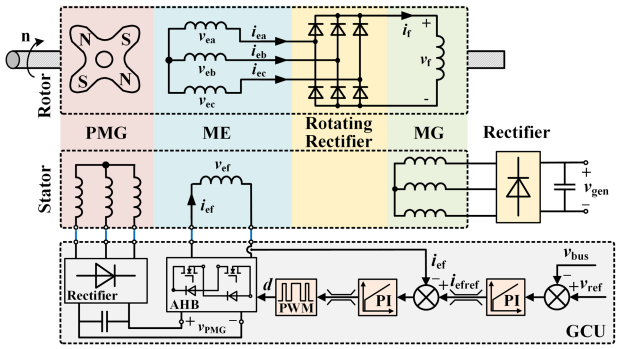

Fig. 2. Structure diagram of a WRSG.

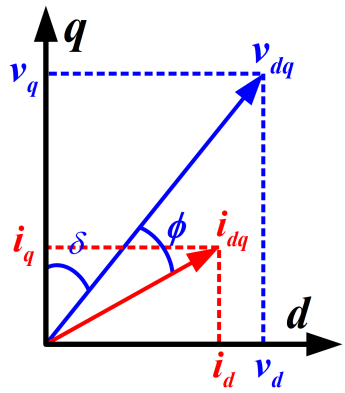

Fig. 3. Space vector diagram of the rectifier bridge.

A structural diagram of a WRSG is shown in Fig. 2. The WRSG consists of a permanent magnet generator (PMG), a main exciter (ME), a rotating rectifier (RR), and a main generator (MG) [29]. All three machines, along with the RR, are mounted coaxially, and the stator is installed within the same casing. The WRSG achieves brushless operation through a two-stage field excitation scheme. The PMG and the asymmetrical half-bridge rectifier provide an independent dc field voltage v_{ef} for the ME. The brushless field system, which includes the ME and RR, supplies the dc field voltage v_{f} to the MG.

A. Small-Signal Impedance Modeling for WRSG

For the small-signal impedance modeling of WRSG, the detailed derivation of the model under single-voltage closed-loop control is given in [12]. Considering the limitations of single-voltage closed-loop control in terms of dynamic performance. In this section, the impedance model of WRSG based on a dual closed-loop control strategy in the *dq*-axis is derived. The voltage equation of the PMG in the *dq*-axis can be expressed as [23]

$$\begin{bmatrix} v_{\mathrm{dP}} \\ v_{\mathrm{qP}} \end{bmatrix} = \begin{bmatrix} L_{\mathrm{dP}}s + R_{\mathrm{sP}} & -\omega_{\mathrm{eP}}L_{\mathrm{qP}} \\ \omega_{\mathrm{eP}}L_{\mathrm{dP}} & L_{\mathrm{qP}}s + R_{\mathrm{sP}} \end{bmatrix} \begin{bmatrix} -i_{\mathrm{dP}} \\ -i_{\mathrm{qP}} \end{bmatrix} + \begin{bmatrix} 0 \\ \omega_{\mathrm{eP}}\phi_{\mathrm{mP}} \end{bmatrix} \tag{1}$$

where v_{dP} and v_{qP} represent the *dq*-axis armature voltages of the PMG, i_{dP} and i_{qP} represent the *dq*-axis armature currents, L_{dP} and L_{qP} are the *dq*-axis inductances, R_{sP} denotes the armature resistance, ω_{ep} is the electrical angular velocity, and ϕ_{mP} represents the permanent magnet flux.

The load current of the PMG is negligible during WRSG operation, so it can be further derived

$$v_{\mathrm{dq}} = \begin{bmatrix} 0 & \omega_{\mathrm{eP}}\phi_{\mathrm{mP}} \end{bmatrix}^{\mathrm{T}}. \tag{2}$$

The dc voltage v_{dcP} of the PMG three-phase output after the rectifier-filter circuit can be approximated as

$$v_{\mathrm{dcP}} \approx \sqrt{3}\,|v_{\mathrm{dq}}| = \sqrt{3}\omega_{\mathrm{eP}}\phi_{\mathrm{mP}}. \tag{3}$$

The ME and MG of the WRSG are wound synchronous machines and their voltage equations and flux linkage equations can be expressed as

$$\begin{bmatrix} v_{\mathrm{d}} \\ v_{\mathrm{q}} \\ v_{\mathrm{f}} \end{bmatrix} = \begin{bmatrix} R_{\mathrm{s}} & & \\ & R_{\mathrm{s}} & \\ & & R_{\mathrm{f}} \end{bmatrix} \begin{bmatrix} -i_{\mathrm{d}} \\ -i_{\mathrm{q}} \\ i_{\mathrm{f}} \end{bmatrix} + s \begin{bmatrix} \psi_{\mathrm{d}} \\ \psi_{\mathrm{q}} \\ \psi_{\mathrm{f}} \end{bmatrix} + \omega_{\mathrm{e}} \begin{bmatrix} -\psi_{\mathrm{q}} \\ \psi_{\mathrm{d}} \\ 0 \end{bmatrix} \tag{4}$$

$$\begin{bmatrix} \psi_{\mathrm{d}} \\ \psi_{\mathrm{q}} \\ \psi_{\mathrm{f}} \end{bmatrix} = \begin{bmatrix} L_{\mathrm{d}} & & L_{\mathrm{md}} \\ & L_{\mathrm{q}} & \\ L_{\mathrm{md}} & & L_{\mathrm{f}} \end{bmatrix} \begin{bmatrix} -i_{\mathrm{d}} \\ -i_{\mathrm{q}} \\ i_{\mathrm{f}} \end{bmatrix} \tag{5}$$

where v_{d}, v_{q}, and v_{f} represent the *dq*-axis armature voltages and field voltage, i_{d},i_{q}, and i_{f} represent the *dq*-axis armature currents and field current, L_{d}, L_{q}, L_{f}, and L_{md} denote the *dq*-axis inductance, field inductance, and *d*-axis mutual inductance, R_{s} and R_{f} the armature and field resistance, ω_{e} is the electrical angular velocity, and ψ_{d}, ψ_{q}, and ψ_{f} are the *dq*-axis flux linking and the field flux linking.

Substituting (5) into (4), the *dq*-axis voltage v_{dq} versus current i_{dq} and field current i_{f} as

$$\hat{v}_{\mathrm{dq}} = \begin{bmatrix} sL_{\mathrm{d}} + R_{\mathrm{s}} & -\omega_{\mathrm{e}}L_{\mathrm{q}} \\ \omega_{\mathrm{e}}L_{\mathrm{d}} & sL_{\mathrm{q}} + R_{\mathrm{s}} \end{bmatrix} \begin{bmatrix} -\hat{i}_{\mathrm{d}} \\ -\hat{i}_{\mathrm{q}} \end{bmatrix} + \begin{bmatrix} sL_{\mathrm{md}} \\ \omega_{\mathrm{e}}L_{\mathrm{md}} \end{bmatrix} \hat{i}_{\mathrm{f}}. \tag{6}$$

And the field current i_{f} versus field voltage v_{f} and *dq*-axis current i_{dq} as

$$\hat{i}_{\mathrm{f}} = \frac{1}{sL_{\mathrm{f}} + R_{\mathrm{f}}}\hat{v}_{\mathrm{f}} + \frac{sL_{\mathrm{md}}}{sL_{\mathrm{f}} + R_{\mathrm{f}}}\hat{i}_{\mathrm{d}}. \tag{7}$$

According to the phase and amplitude relationship between the dc voltage v_{gen} and *dq*-axis voltage v_{dq} of MG in Fig. 3, which can be derived as [30]

$$\begin{cases} \hat{v}_{\mathrm{gen}} = K_{\mathrm{v}}\hat{v}_{\mathrm{dq}} \\ \hat{i}_{\mathrm{dq}} = K_{\mathrm{i}}\hat{i}_{\mathrm{gen}} \end{cases} \tag{8}$$

where i_{gen} is the rectified output current of the WRSG, K_{v} and K_{i} represent the voltage coefficient matrix and current system matrix of the rectifier bridge, respectively, which can be denoted as

$$\begin{cases} K_{\mathrm{v}} = k_{\mathrm{v}}[\sin\delta, \cos\delta] \\ K_{\mathrm{i}} = [\sin(\delta+\phi), \cos(\delta+\phi)]/k_{\mathrm{i}} \end{cases} \tag{9}$$

where k_{v} and k_{i} denote the voltage and current coefficients of the rectifier bridge, respectively, ϕ and δ are the power factor angle and the power angle of the MG, respectively.

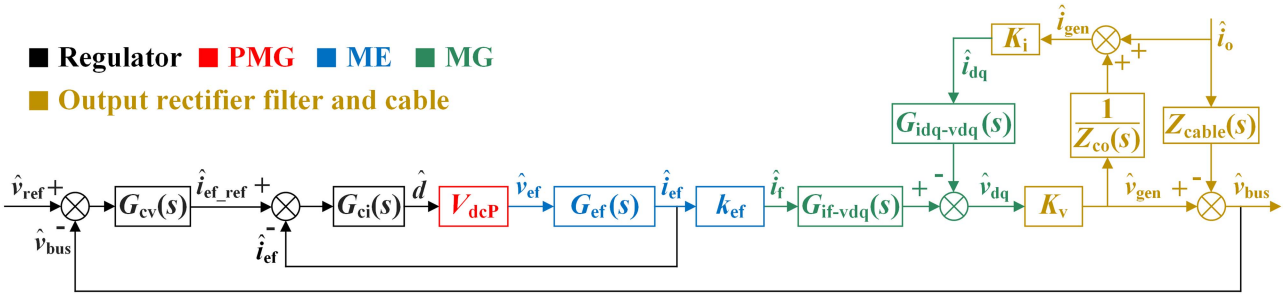

Fig. 4. Small-signal impedance model block diagram of WRSG-based HVDC power supply system.

To improve the dynamic performance of the WRSG, the current linear amplifier characteristic of the brushless field system can be achieved by optimizing the commutation reactance of the ME during the electromagnetic design process of the WRSG [31], [32]. The ratio of the MG field current to the ME field current remains essentially constant when the operating temperature and load change, which can be expressed as

$$\hat{i}_f = f\left(\hat{i}_{ef}\right) = k_{ef}\hat{i}_{ef} \tag{10}$$

where k_{ef} is the amplifier characteristic gain of ME.

Using the above characteristics simplifies the system impedance model while maintaining its accuracy, and also facilitates the design of closed-loop control parameters.

It is noteworthy that, the generator on an aircraft is usually placed on the engine side, while the dc bus is situated in the fuselage. The parasitic impedance of the long transmission cable between them should not be ignored. Additionally, to ensure accurate voltage regulation on the bus, the voltage sampling point, i.e., the regulation point (POR), of the in-service aircraft is located at the dc bus. Therefore, the relationship between the WRSG voltage v_{gen} and dc bus voltage v_{bus} as well as the i_{gen} and i_{dc} can be derived as

$$\begin{cases} \hat{i}_o = \hat{i}_{gen} - \hat{i}_{co} \\ \hat{v}_{bus} = \hat{v}_{gen} - \hat{i}_{dc}Z_{cable} \end{cases}. \tag{11}$$

As a result of the abovementioned analysis, the block diagram of the small-signal impedance model, as shown in Fig. 4, is obtained.

B. Control Parameter Design

For the field current inner loop, based on Fig. 4, the open-loop transfer function $G_{iopen}(s)$ can be expressed as

$$G_{iopen}(s) = G_{ci}(s)V_{dcP}G_{ef}(s) \tag{12}$$

where $G_{ci}(s)$ denotes the transfer function of the field current PI regulator and $G_{ef}(s)$ is the transfer function from field voltage to current.

The zeros of the PI regulator are usually set to offset the poles, thus, the field current inner loop is generally designed as a first-order system. The closed-loop transfer function can be written as

$$G_{iclose}(s) = \omega_{ci}/(s + \omega_{ci}) \tag{13}$$

where ω_{ci} is the current loop bandwidth, which can be taken as 1/5 to 1/20 of the switching frequency.

Combining (13), (A1), and (A2), the proportional gain k_{pi} and the integral gain k_{ii} of the field current inner loop regulator can be set to

$$\begin{cases} k_{pi} = \omega_{ci}L_{ef}/\sqrt{3}\omega_{eP}\phi_m \\ k_{ii} = \omega_{ci}R_{ef}/\sqrt{3}\omega_{eP}\phi_m \end{cases}. \tag{14}$$

For the voltage loop design, it can be considered as a typical second-order system. Therefore, the proportional gain k_{pv} and the integral gain k_{iv} of the voltage loop regulator can be designed as

$$\begin{cases} k_{pv} = \frac{a_1a_3 - a_1\omega_n\xi + a_2\omega_n^2}{2a_1a_2\omega_n\xi - a_1^2 - a_2^2\omega_n^2} \\ k_{iv} = \frac{\omega_n^2}{a_1} + \frac{a_1a_2a_3\omega_n^2 - a_1a_2\omega_n^3\xi + a_2^2\omega_n^4}{2a_1^2a_2\omega_n\xi - a_1^3 - a_1a_2^2\omega_n^2} \end{cases} \tag{15}$$

where ω_n is the natural frequency, ξ is the damping ratio, which is typically chosen between 0.6 and 0.8 to ensure optimal performance of the second-order system, and a_1, a_2, and a_3 are defined as

$$\begin{cases} a_1 = \omega_e k_{ef}\omega_{ci}k_vL_{md}\cos\delta \\ a_2 = k_{ef}\omega_{ci}k_vL_{md}\sin\delta \\ a_3 = \omega_{ci} \end{cases}. \tag{16}$$

And the relationship between the natural frequency ω_n and the voltage loop bandwidth ω_{cu} can be expressed as

$$\omega_n = \frac{\omega_{cu}}{\sqrt{1 - 2\xi^2 + \sqrt{2 - 4\xi^2 + 4\xi^4}}}. \tag{17}$$

C. Output Impedance of the WRSG-Based HVDC Power Supply System

Based on Fig. 4, the WRSG output impedance $Z_{out}(s)$, defined as the closed-loop transfer function from the output current $i_o(s)$ to the bus voltage $v_{bus}(s)$, can be expressed as

$$\begin{aligned} Z_{out}(s) &= -\frac{\hat{v}_{bus}(s)}{\hat{i}_o(s)} \\ &= \frac{Z_{cable}(s)\left(1 + \frac{K_vG_{idq-vdq}(s)K_i}{Z_{co}(s)}\right) + K_vG_{idq-vdq}(s)K_i}{1 + k_{ef}G_{cv}(s)G_{iclose}(s)K_vG_{if-vdq}(s) + \frac{K_vG_{idq-vdq}(s)K_i}{Z_{co}(s)}} \end{aligned} \tag{18}$$

where $Z_{cable}(s)$ and $Z_{co}(s)$ denote the transfer functions of the line impedance and the output capacitance, respectively, which

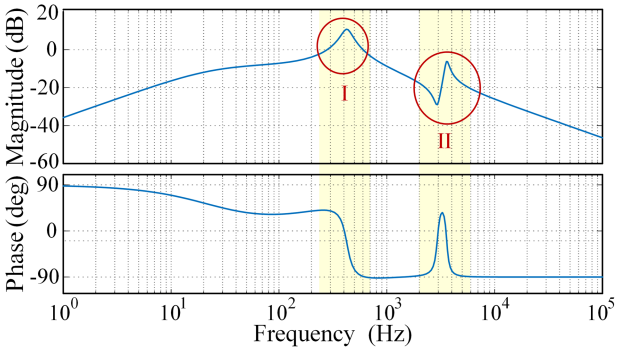

Fig. 5. Bode diagram of $Z_s(s)$.

TABLE I
PARAMETERS OF THE 90 KW WRSG

Symbol	Definition	Value
P_{WRSG}	Rated power	90 kW
n_{WRSG}	Rated speed	8000 r/min
f_{MG}	Fundamental frequency of MG	400 Hz
ω_{ep}	Electrical angular velocity of PMG	837.76 rad/s
ϕ_{mP}	Permanent magnet magnetic flux of PMG	0.00465
L_d	D-axis inductance of MG in WRSG	233.16 μH
L_q	Q-axis inductance of MG in WRSG	121.98 μH
L_f	Field inductance of MG in WRSG	46.17 mH
R_s	Armature of MG in WRSG	10.37 mΩ
R_f	Field resistance of MG in WRSG	420.55mΩ
k_{ef}	Amplifier characteristic gain of ME	3.35
k_{if}	Ratio of output current to field current	27.80
C_o	WRSG output capacitance	300 μF
C_{bus}	Dc bus filter capacitance	600 μF
L_{cable}	Cable inductance	10 μH
R_{cable}	Cable resistance	20 mΩ
f_s	Switching frequency	10 kHz
ω_{ci}	Field current loop bandwidth	1 kHz

can be expressed as

$$\begin{cases} Z_{cable}(s) = sL_{cable} + R_{cable} \\ Z_{co}(s) = 1/sC_o \end{cases} \tag{19}$$

where $L_{cable}(s)$ and $R_{cable}(s)$ are the cable's parasitic inductance and resistance, and C_o is the output capacitance of the WRSG.

A filter capacitor C_{bus} is typically placed on the dc bus side. The total source subsystem output impedance $Z_s(s)$ can then be expressed as

$$Z_s(s) = \frac{1}{sC_{bus}} // Z_{out}(s). \tag{20}$$

Fig. 5 presents the output impedance Bode diagram of a typical WRSG-based HVDC power supply system, based on the parameters provided in Table I. The diagram reveals two resonance peaks in the output impedance: one in the mid-frequency range (100–500 Hz) and the other in the high-frequency range.

The impedance spike within the mid-frequency range is caused by the inductive resistance characteristics of the WRSG combined with the three-phase output rectified filter capacitance. While the resonance peak in the high-frequency band results from the interaction between the cable parasitic impedance and the bus capacitance. Furthermore, it is clarified that the amplitude of the resonance spike in the high-frequency band is typically small, owing to the large capacitance of the bus capacitor. Consequently, the primary cause of system instability under CPL conditions is the impedance spike in the mid-frequency band.

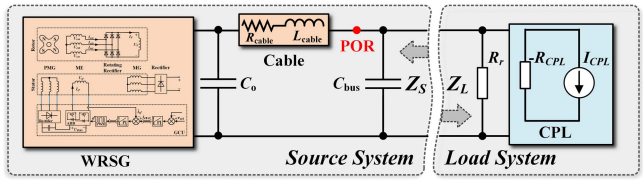

Fig. 6. Equivalent block diagram of a single-channel WRSG-based HVDC system.

III. Proposed Adaptive Active Damping Control Strategy

A. Stability Analysis of the WRSG-Based HVDC Power Supply System Under CPL Operation

Before discussing methods to enhance stability, this section analyzes the stability of the WRSG-based HVDC system in Fig. 6, and explores the influence of system parameters on stability.

Electrical equipment on board can be divided into linear loads and nonlinear loads based on their operating characteristics. Linear loads are mostly resistive loads, while nonlinear loads are primarily CPL. Therefore, the load subsystem considers both resistive loads and CPL. The input impedance $Z_{in\_r}(s)$ of a resistive load can be written as

$$Z_{in\_r}(s) = R_r = V_{bus}^2/P_r \tag{21}$$

where R_r and P_r denote the resistance and power of the resistive load, respectively.

The CPL, linearized around the operating point, can be approximated as a negative impedance in parallel with a current source [20], [21]. Its input impedance $Z_{in\_CPL}(s)$ can be written as

$$Z_{in\_CPL}(s) = -R_{CPL} = -V_{bus}^2/P_{CPL} \tag{22}$$

where R_{CPL} and P_{CPL} represent the resistance and power of the CPL, respectively. Thus, the input impedance $Z_L(s)$ of the load subsystem can be expressed as

$$Z_L(s) = Z_{in\_CPL}(s) // Z_{in\_r}(s) = \frac{-V_{bus}^2}{P_{CPL} - P_r}. \tag{23}$$

It is evident that when $P_{CPL} > P_r$, the load subsystem as a whole exhibits a negative impedance characteristic.

Before the stability analysis, the stability criterion is given here. For the typical cascade system shown in Fig. 6. The stability of interactions in cascaded systems is commonly assessed using impedance-based stability criteria. Specifically, the Nyquist criterion is generally applied to analyze the interaction between the source and load subsystems [13], [16], [22]. For stable system operation, the following two conditions must be satisfied.

1) The output impedance of the source subsystem Z_s does not intersect with the input impedance of the load subsystem, Z_L, and Z_s remains consistently lower than Z_L. This aligns with the principles of the Middlebrook criterion.

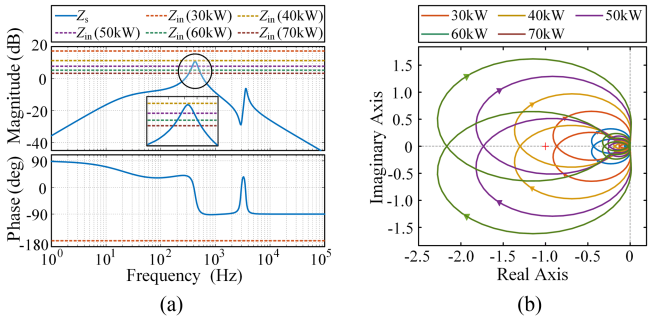

Fig. 7. Results of stability analysis for different CPL values. (a) Bode diagram of Z_s and Z_{in}. (b) Nyquist curve of Z_s/Z_L.

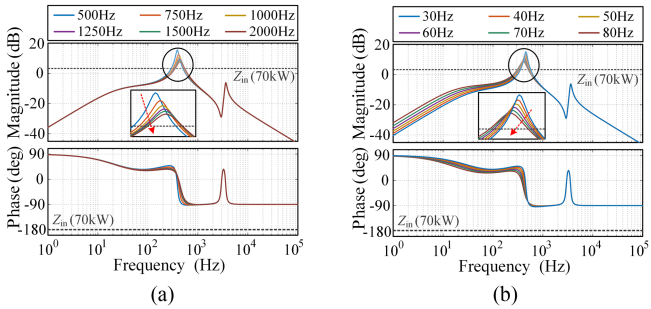

Fig. 8. Bode diagrams of Z_s for different bandwidths. (a) Field current loop. (b) Voltage loop.

2) If Z_s and Z_L intersect, the phase difference between them must be less than 180° to satisfy the Middlebrook criterion.

The stability of the cascaded system can also be assessed by verifying that the impedance ratio, represented by the Nyquist curve of Z_s/Z_L, does not encircle the point (-1, 0).

To analyze the impact of the load on system stability. Consider the load conditions under typical flight profiles. The resistive load is set to remain at 20 kW, while the CPL is varied from 20 kW to 70 kW.

The bode diagram of source impedance and load impedance are shown in Fig. 7(a). It is observed that when P_{cpl} increases to 40 kW, Z_s and Z_L intersect, and the phase difference at the intersection frequency exceeds 180°, which does not satisfy the stability criterion. This is also evident in the Nyquist curve shown in Fig. 7(b).

B. Limitations of the Traditional Control Methods

To further analyze the impact of control parameters on system stability. Fig. 8 shows the bode diagrams of Z_S at different current loop and voltage loop bandwidths. It can be seen that increasing the bandwidth slightly reduces the impedance peak of Z_S , but the impedance still intersects with Z_L . This indicates that optimizing the control parameters alone cannot completely eliminate the risk of system instability.

C. Analysis of Active Damping Positions and Configurations

Given the special application environment and stringent requirements of aircraft EPS, adding an active damping control strategy on the source subsystem is more practical than optimizing the control strategy for each CPL, and also easier for expansion of the system. This section investigates the active damping control strategy for the source subsystem to enhance stability in the presence of CPL.

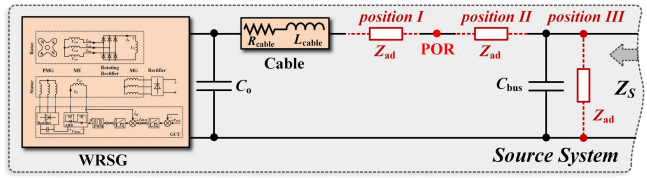

Fig. 9. Schematic diagram of active damping position.

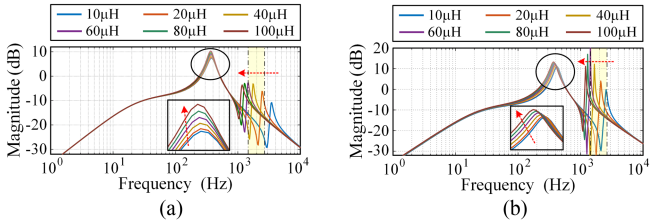

Fig. 10. Bode diagrams of Z_s with different L_{cable}. (a) Preside. (b) Postside.

The essential of the active damping control strategy is to damp the impedance peaks of Z_s by adding a virtual impedance either in series or parallel with the system, thus avoiding intersection with the Z_L. Given the implementation of closed-loop control for active damping in WRSG, the virtual impedance is ideally placed at the voltage or current sampling points to facilitate the derivation of the active damping function.

Additionally, the peak output impedance of the WRSG-based HVDC power supply system occurs in the mid-frequency band. Since, the voltage loop bandwidth of the WRSG closed-loop control cannot cover this frequency range, active damping control must be implemented through the field current loop. This is achieved by sampling the bus voltage and integrating it with the virtual impedance, where the voltage sampling point is the POR. Based on this, Fig. 9 illustrates three potential positions for placing the virtual impedance: the preside and postside of the POR, and the filter capacitor C_{bus} side.

The impedance Z_{ad} for active damping can be implemented using resistance, inductance, capacitance, or a combination of these elements.

Specifically, resistors can be placed either in series on the pre- and postside of the POR or in parallel on the bus side.

Capacitors, due to their ability to pass high frequencies and block low frequencies, are only suitable for parallel placement and cannot be used in series configurations.

Inductors, which allow low frequencies to pass while blocking high frequencies, are only suitable for series placement and cannot be used in parallel configurations. Furthermore, connecting inductors in series at the POR is equivalent to increasing the parasitic inductance in the line impedance. This not only fails to attenuate the mid-frequency impedance spike but also shifts the high-frequency resonance peak toward the lower frequency band, as illustrated in Fig. 10. After the output voltage of the

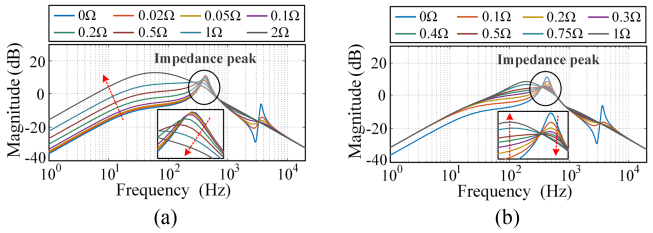

Fig. 11. Bode diagrams of Z_s with different R_{ad}. (a) Preside. (b) Postside.

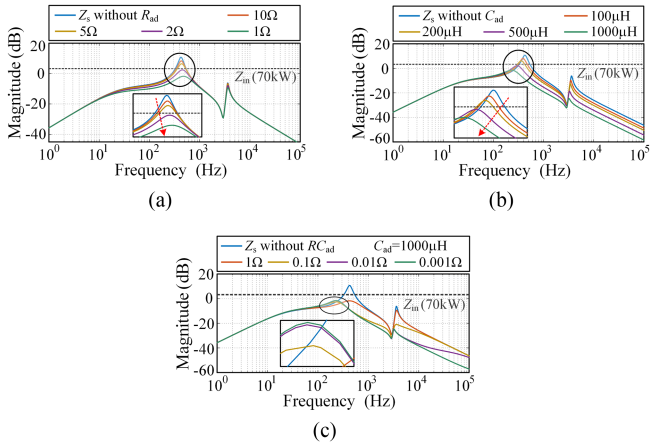

Fig. 12. Bode diagram of Z_s with different virtual impedances in parallel connection. (a) Virtual resistance R_{ad}. (b) Virtual capacitance C_{ad} (c) Virtual resistance-capacitance series RC_{ad}.

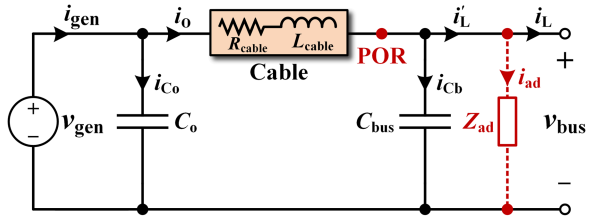

Fig. 13. Equivalent circuit diagram after adding virtual impedance Z_{ad}.

WRSG passes through the uncontrolled rectifier circuit, a six-frequency ripple is introduced in the dc voltage, corresponding to a frequency of 2.4 kHz (6×400 Hz) under the operating condition at rated speed (8000 r/min). Although the amplitude of this ripple is reduced by capacitive filtering, the movement of the high-frequency resonance peak into this frequency range can significantly amplify the voltage ripple, adversely affecting system operation.

In summary, the series inductor configuration is not suitable as a standalone damping element. It can only serve as an auxiliary component in parallel with the damping resistor to mitigate the voltage drop induced by the resistor.

In summary, the virtual impedance on the pre-side of the POR only considers resistance. For the postside of the POR, virtual impedance is implemented as a parallel combination of resistance and inductance. This approach addresses the issue of bus voltage drop caused by a series-connected resistor alone, as the parallel inductor compensates for the voltage drop. For parallel virtual impedance on the bus filter capacitor C_{bus} side, options include capacitors, resistors, and resistor-capacitor series configurations.

Fig. 11(a) shows the bode diagrams of Z_s with different R_{ad} in series on the preside of the POR. And the variations in impedance spikes within the mid-frequency band for different values of R_{ad} are highlighted and zoomed in the figure. When the R_{ad} is small, the peak impedance of Z_s does not change much, and the resonance peak in the high-frequency band decreases. This is because R_{ad} damps the LC filter formed by L_{cable} and C_{bus}. However, as R_{ad} gradually increases, the impedance peak of Z_s first decreases and then shifts towards the low-frequency band. This is equivalent to increasing the output impedance of the WRSG due to closed-loop control. This proposal increases the risk of system instability in the low-frequency region.

For the solution with virtual impedance in series at the post-side of the POR, a 1 mH virtual inductor is connected in parallel with R_{ad} to avoid voltage drop, thus maintaining high regulation accuracy. The bode diagram of Z_s for different R_{ad} is shown in Fig. 11(b). This method has a limited effect on the rejection of Z_s impedance peaks. Similar to the preside configuration, a new impedance spike appears in the mid-frequency band. Therefore, this solution is also not suitable as an active damping control strategy.

Finally, the active damping solution on the C_{bus} side is analyzed. Three types of virtual impedance can be selected: 1) resistance (R), 2) capacitance (C), and 3) resistance-capacitance (RC) series. The bode diagrams of Z_s for different virtual impedance parameters in three forms are shown in Fig. 12. All three methods are effective for impedance peak rejection. However, their overall impact on the system, when integrated into the active damping control strategy, requires further derivation, and analysis.

D. Derivation of Active Damping Control Strategy

In system operation, active damping is achieved by adding a loop to the closed-loop control strategy. Based on the analysis in Section III-C, the field current loop is selected as its position.

In the equivalent circuit diagram given in Fig. 13, the current expressions for each node in the system with active damping can be derived as

$$\begin{cases} \hat{i}'_{\mathrm{L}} = \hat{i}_{\mathrm{L}} + \frac{\hat{v}_{\mathrm{bus}}}{Z_{\mathrm{ad}}} \\ \hat{i}'_{\mathrm{o}} = \hat{i}'_{\mathrm{L}} + \frac{\hat{v}_{\mathrm{bus}}}{Z_{\mathrm{cbus}}} \\ \hat{i}'_{\mathrm{gen}} = \hat{i}'_{\mathrm{o}} + \frac{(\hat{i}'_{\mathrm{o}} Z_{\mathrm{cable}} + \hat{v}_{\mathrm{bus}})}{Z_{\mathrm{co}}} \end{cases} \tag{24}$$

where i_L is the load current, Z_{ad} is the virtual impedance, and Z_{co} and Z_{bus} denote the impedances of the output filter capacitor and bus filter capacitor, respectively. Thus, the expression for the WRSG output current, both before and after adding the active damping control strategy, is then derived as

$$\begin{cases} \hat{i}'_{\mathrm{gen}} = (\hat{i}_{\mathrm{L}} + \frac{\hat{v}_{\mathrm{bus}}}{Z_{\mathrm{ad}}} + \frac{\hat{v}_{\mathrm{bus}}}{Z_{\mathrm{cbus}}})(1 + \frac{Z_{\mathrm{cable}}}{Z_{\mathrm{co}}}) + \frac{\hat{v}_{\mathrm{bus}}}{Z_{\mathrm{co}}} \\ \hat{i}_{\mathrm{gen}} = (\hat{i}_{\mathrm{L}} + \frac{\hat{v}_{\mathrm{bus}}}{Z_{\mathrm{cbus}}})(1 + \frac{Z_{\mathrm{cable}}}{Z_{\mathrm{co}}}) + \frac{\hat{v}_{\mathrm{bus}}}{Z_{\mathrm{co}}} \end{cases}. \tag{25}$$

The change in ME field current Δi_{ef} can be obtained as

$$\Delta\hat{i}_{\mathrm{ef}} = \frac{\Delta\hat{i}_{\mathrm{gen}}}{k_{\mathrm{if}}} = \frac{\hat{i}'_{\mathrm{gen}} - \hat{i}_{\mathrm{gen}}}{k_{\mathrm{if}}} = \frac{\hat{v}_{\mathrm{bus}}}{k_{\mathrm{if}} Z_{\mathrm{ad}}}\left(1 + \frac{Z_{\mathrm{cable}}}{Z_{\mathrm{co}}}\right) \tag{26}$$

where k_{if} is the ratio of the output current to the field current. Thus, the active damping expression $G_{\mathrm{ad}}(s)$ can be written as

$$G_{\mathrm{ad}}(s) = \frac{1}{k_{\mathrm{if}} Z_{\mathrm{ad}}}\left(1 + \frac{Z_{\mathrm{cable}}}{Z_{\mathrm{co}}}\right) = \frac{1 + sC_{\mathrm{o}}R_{\mathrm{cable}} + s^2 L_{\mathrm{cable}} C_{\mathrm{o}}}{k_{\mathrm{if}} Z_{\mathrm{ad}}}. \tag{27}$$

The voltage drop is primarily due to the resistance R_{cable} in the line impedance. Ignoring the effect of the inductance L_{cable}, $G_{\mathrm{ad}}(s)$ can be simplified as follows:

$$G_{\mathrm{ad}}(s) = \frac{1 + sC_{\mathrm{o}}R_{\mathrm{cable}}}{k_{\mathrm{if}} Z_{\mathrm{ad}}}. \tag{28}$$

Substituting the three forms of the active damping expression into (28) yields

$$\begin{cases} G_{\mathrm{ad\_r}}(s) = \frac{1}{k_{\mathrm{if}} R_{\mathrm{ad}}}(1 + sC_{\mathrm{o}}R_{\mathrm{cable}}) \\ G_{\mathrm{ad\_c}}(s) = \frac{sC_{\mathrm{ad}}}{k_{\mathrm{if}}}(1 + sC_{\mathrm{o}}R_{\mathrm{cable}}) \\ G_{\mathrm{ad\_cr}}(s) = \frac{1}{k_{\mathrm{if}}}\frac{sC_{\mathrm{ad}}}{1 + sR_{\mathrm{ad}}C_{\mathrm{ad}}}(1 + sC_{\mathrm{o}}R_{\mathrm{cable}}) \end{cases}. \tag{29}$$

The active damping function based on virtual resistance contains a constant term of $1/k_{\mathrm{if}}R_{\mathrm{ad}}$. This is equivalent to adding a feedforward control at the field current inner loop. As shown in Fig. 12(a), the corresponding R_{ad} acts as a powerful feedforward control parameter, which is much larger than the required field current, affecting the transient response of the system. This adversely impacts the system's performance, rendering the active damping control strategy based on virtual resistance unsuitable for implementation.

Active damping functions based on virtual C and virtual RC include a second-order derivative term. This can increase the noise introduced by the measuring elements in practical control. To address this issue, it is observed that for (29), when the condition $R_{\mathrm{ad}}C_{\mathrm{ad}} = C_{\mathrm{o}}R_{\mathrm{cable}}$ is satisfied, the $G_{\mathrm{ad\_cr}}(s)$ can be further simplified to a first-order derivative term as

$$G_{\mathrm{ad\_cr}}(s) = \frac{sC_{\mathrm{ad}}}{k_{\mathrm{if}}}. \tag{30}$$

As the value of R gradually decreases, the impedance peak shifts toward the lower frequency band, eventually converging to the behavior observed in virtual C control, as demonstrated in Fig. 12(c). However, the amplitude of the impedance peak remains largely unchanged, indicating that the system's stability under CPL conditions is unaffected. In other words, the stability of the system under virtual RC control is insensitive to variations in R_{ad}. Thus, only the value of C_{ad} needs to be considered when designing the active damping function. Ultimately, the virtual RC configuration is selected as the active damping control strategy.

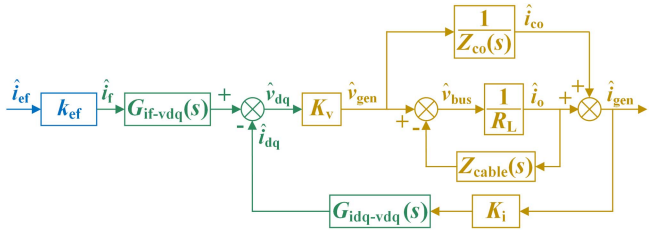

Fig. 14. Small-signal model of k_{if}.

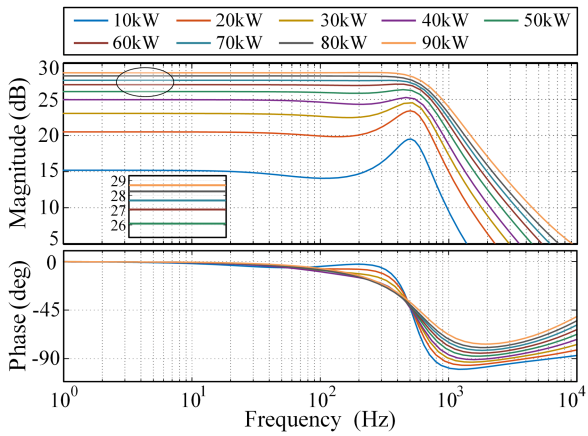

Fig. 15. Bode diagram of $k_{\mathrm{if}}(s)$ under full load conditions.

E. Active Damping Parameter Selection

As indicated by (30), the strength of the active damping control strategy is determined by k_{if} and C_{ad}, where the magnitude of k_{if} is influenced by the characteristics of the WRSG. Based on the impedance model of the WRSG illustrated in Fig. 4, a small-signal model of $k_{\mathrm{if}}(s)$ is presented in Fig. 14. By deriving the closed-loop transfer function from i_{ef} to i_{gen}, $k_{\mathrm{if}}(s)$ can be obtained and expressed as

$$k_{\mathrm{if}}(s) = \frac{\hat{i}_{\mathrm{gen}}(s)}{\hat{i}_{\mathrm{ef}}(s)} = \frac{\frac{k_{\mathrm{ef}}K_{\mathrm{v}}G_{\mathrm{idq-vdq}}(s)}{R_{\mathrm{L}}} + \frac{k_{\mathrm{ef}}K_{\mathrm{v}}G_{\mathrm{idq-vdq}}(s)}{Z_{\mathrm{co}}(s)}\left(1 + \frac{Z_{\mathrm{cable}}(s)}{R_{\mathrm{L}}}\right)}{1 + \frac{Z_{\mathrm{cable}}(s)}{R_{\mathrm{L}}} + \frac{K_{\mathrm{v}}G_{\mathrm{idq-vdq}}(s)K_{\mathrm{i}}}{Z_{\mathrm{co}}(s)} + \frac{K_{\mathrm{v}}G_{\mathrm{idq-vdq}}(s)K_{\mathrm{i}}}{R_{\mathrm{L}}}}. \tag{31}$$

Given the pronounced nonlinear characteristics of the WRSG, the analysis of $k_{\mathrm{if}}(s)$ should encompass the full load operating range of the WRSG. Fig. 15 presents the bode diagram of $k_{\mathrm{if}}(s)$ as the load R_{L} varies from 10 kW to 90 kW.

It can be observed that under specific load conditions, $k_{\mathrm{if}}(s)$ exhibits a constant amplitude in the mid-to-low frequency range, which corresponds to the gain from field current to output current at the current load. A gradual attenuation trend emerges with increasing frequency, attributed to the combined effects of the WRSG, cable impedance, and output capacitance. In the design of the active damping function $G_{\mathrm{ad}}(s)$, it is sufficient to consider only the gain in the mid-to-low frequency band in $k_{\mathrm{if}}(s)$. As the load gradually increases, a corresponding increase in the

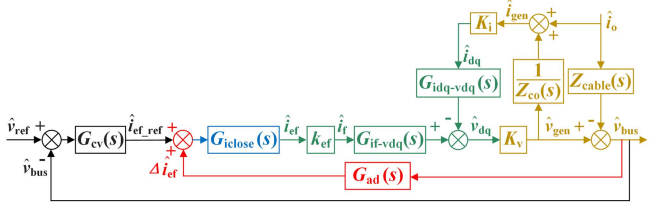

Fig. 16. Small-signal block diagram with active damping control strategy.

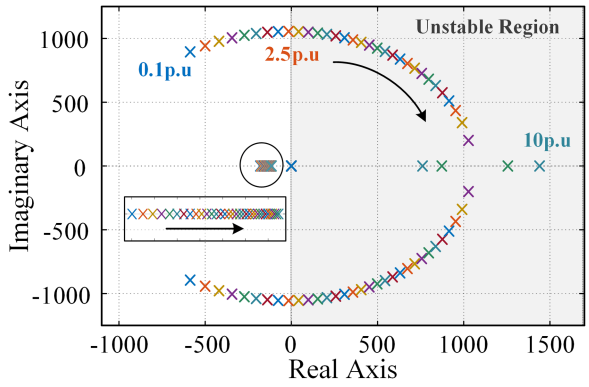

Fig. 17. Dominant pole diagram of G_{v_ad} for different C_{ad}.

gain of $k_{if}(s)$ is observed, as illustrated in Fig. 15. This behavior needs to be considered in the subsequent parameterization of $G_{ad}(s)$.

In theory, increasing the value of the virtual capacitor C_{ad} can enhance the stability margin. However, its impact on closed-loop regulation must also be considered. Therefore, the stability of the voltage-closed loop with the active damping control strategy is analyzed. Fig. 16 presents the updated small-signal control block diagram, and the closed-loop transfer function can be expressed as follows:

$$G_{v\_ad}(s) = \frac{\hat{v}_{dc}(s)}{\hat{v}_{ref}(s)} = \frac{k_{ef}G_{cv}(s)G_{i\_close}(s)K_vG_{if-vdq}(s)}{1+k_{ef}G_{cv}(s)G_{iclose}(s)K_vG_{if-vdq}(s)- k_{ef}G_{ad}(s)G_{iclose}(s)K_vG_{if-vdq}(s)+\frac{K_vG_{idq-vdq}(s)K_i}{Z_{co}(s)}}. \quad (32)$$

Fig. 17 illustrates the dominant pole distribution of G_{v_ad} under different C_{ad}. It is observed that as C_{ad} increases to 2.5 p.u. (where 1 p.u. is equivalent to 1000 μF), a pole appears in the right half-plane, which indicates a potential instability in the closed-loop system. The results indicate that increasing the active damping strength adversely affects loop stability. By combining the variation trend of $k_{if}(s)$ under full load conditions, as illustrated in Fig. 15, with the impact of CPL on impedance stability, as shown in Fig. 7. Fig. 18 further summarizes the stability boundaries of the system under various CPL conditions. Based on this analysis, the region of active damping coefficient values required for stable system operation under full load conditions has been determined. Selecting a value within this region ensures both the stable operation of the system with CPL and the stability of the closed-loop control.

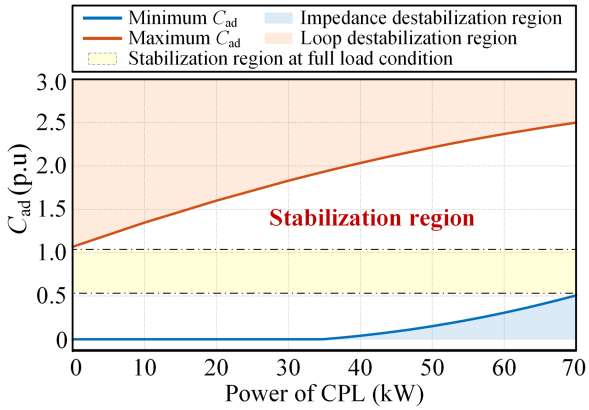

Fig. 18. Schematic diagram of the system stability boundaries under various CPL conditions.

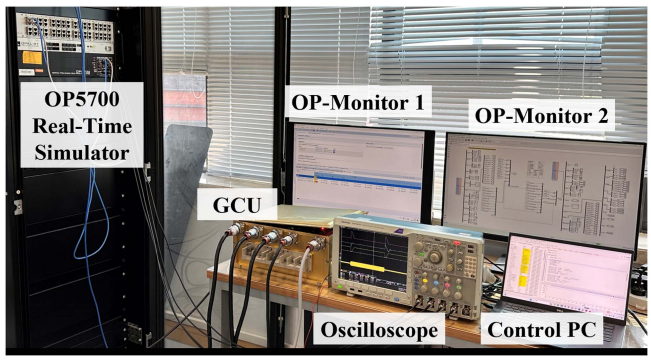

Fig. 19. HIL platform.

IV. Experimental Verification

To invalidate the proposed active damping control strategy and the accuracy of the theoretical analysis, a hardware-in-the-loop (HIL) platform is built, as shown in Fig. 19. The experimental platform consists of the OP5700 real-time simulator and the generator control unit (GCU).

The power components, including the WRSG and CPL, are implemented in the OP5700 real-time simulator, which features 8 CPU cores and achieves simulation steps of 10 μs, enabling real-time, high-fidelity representation of the system's operational state. While the proposed control strategy is realized in GCU, which includes AD sampling module, signal conditioning module, and dsp-based control module. The parameters are detailed in Table I.

A. Validation of the Impedance Model

To verify the accuracy of the proposed impedance model, a 270 V/90 kW HVDC WRSG is used as a case study. A time-domain simulation model of the source subsystem is developed in MATLAB/Simulink. Using the OPAL-RT HIL system, the impedance characteristics of the model were extracted by employing the sweep frequency method [33]. An ideal current source containing a dc and an additional ac sinusoidal disturbance current is connected in parallel to the dc side as a load.

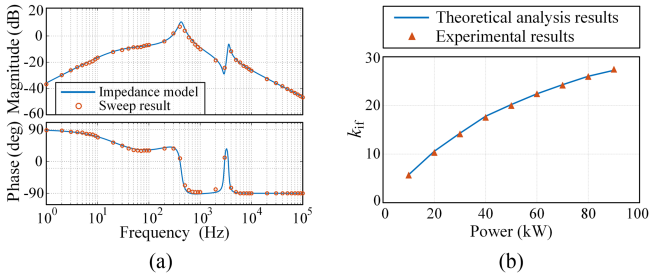

Fig. 20. Comparison of theoretical analysis and experimental. (a) Impedance modeling of WRSG-based HVDC power supply system. (b) Small-signal model of k_{if} (s).

By measuring the output voltage and current of the source subsystem, the output impedance at each frequency can be calculated. Fig. 20(a) compares the impedance model with the actual sweep results from 1 Hz to 10^5 kHz. It can be observed that the proposed impedance model closely matches the sweep results, thereby verifying the accuracy of the derived impedance model.

Similarly, Fig. 20(b) compares the theoretical and experimental values of $k_{if}(s)$ for each load power. The accuracy of the derived $k_{if}(s)$ small-signal model is verified.

B. Operating Conditions of WRSG-Based HVDC Power Supply System With CPL

Consistent with the theoretical analysis of typical load conditions, the resistive load power is maintained at 20 kW. Fig. 21(a) presents the waveforms of dc bus voltage, total load current, resistive load current, and CPL current for progressively increasing CPL power.

The partially expanded waveforms are shown in Fig. 21(b), (c), and (d). As the CPL reaches 45 kW and above, the system exhibits significant instability. The amplitude of the instability gradually increases with the value of the CPL, eventually leading to system breakdown.

Furthermore, under the operating condition with the resistive load maintained at 20 kW and CPL set to 60 kW, Fig. 22 presents the waveforms of each observation point in the system as the bandwidths of the field current inner loop and voltage outer loop are varied. The results demonstrate that increasing the control bandwidth can suppress system oscillations, but the degree of suppression is limited, and the effectiveness diminishes as the bandwidth increases. This is consistent with the theoretical analysis in Section III-B. Thus, the limitation of PI control in improving the stability of the system is illustrated.

C. Effect of the Proposed Active Damping Control Strategy

Under the same load conditions, Fig. 23 illustrates the waveforms at each observation point when the proposed virtual *RC*-based active damping control strategy is applied. The results demonstrate that enabling the active damping strategy transitions the system from oscillatory instability to stable operation, thereby verifying the effectiveness of the proposed approach.

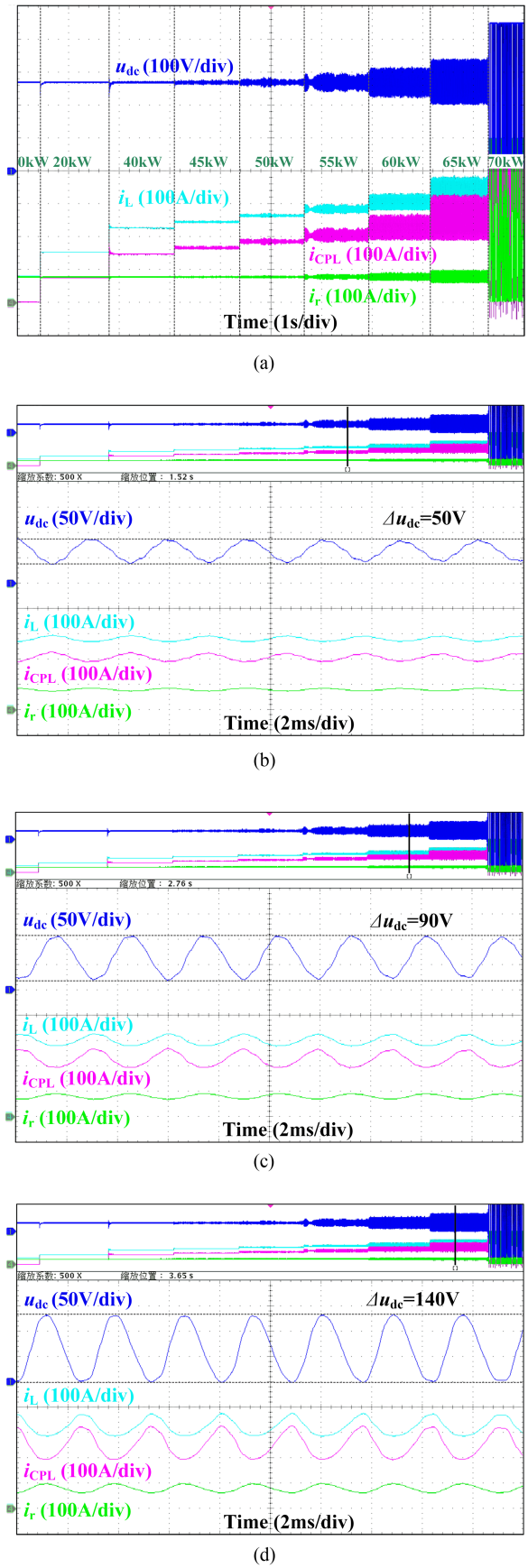

Fig. 21. Experimental results when gradually increasing the value of P_{CPL}. (a) Overall waveforms. (b) Zoomed view of the P_{CPL} value 55. (c) Zoomed view of the P_{CPL} value 60. (d) Zoomed view of the P_{CPL} value 65.

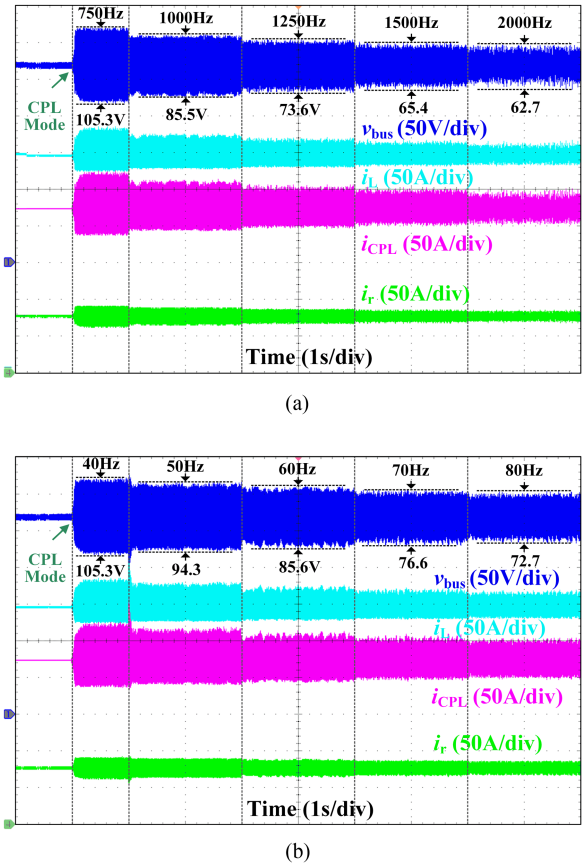

Fig. 22. Experimental results when gradually changing the control bandwidths. (a) Field current loop. (b) Voltage loop.

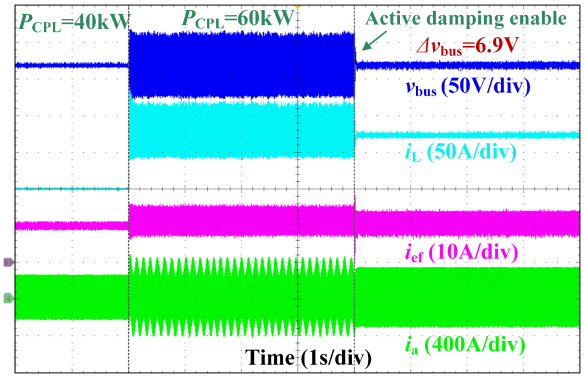

Fig. 23. Experimental results using the proposed virtual *RC*-based active damping control strategy.

Furthermore, Fig. 24 provides an expanded view of the waveforms at each observation point under the virtual *R*- and virtual *C*-based active damping control strategies. When the virtual *R*-based active damping is enabled, a significant voltage transient occurs at the initial instant, reaching 240.8 V, as shown in Fig. 24(a). In contrast, while the virtual *C*-based active damping avoids this issue, it introduces steady-state noise burrs, as illustrated in Fig. 24(b). These are consistent with the theoretical analysis in Section III-D.

In summary, the proposed virtual *RC*-based active damping control strategy exhibits superior performance in both transient

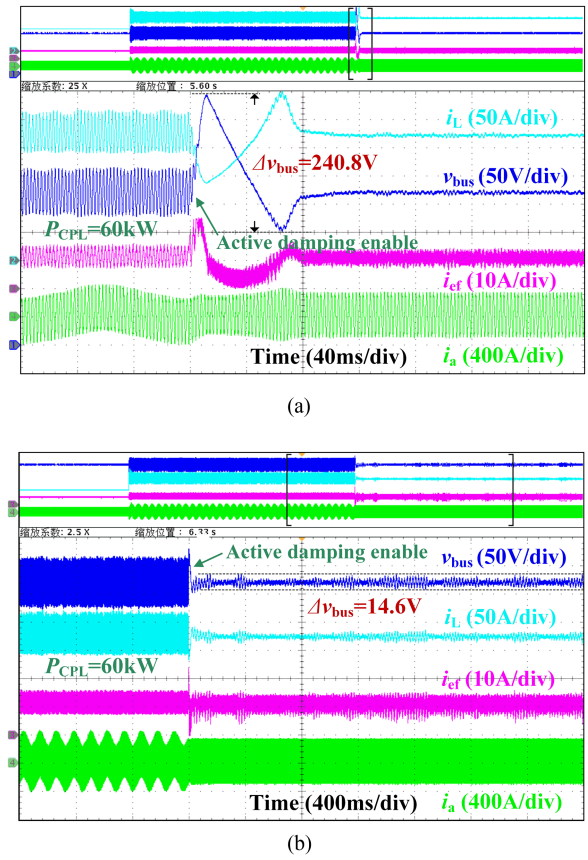

Fig. 24. Experimental results for different virtual impedances. (a) Virtual *R*. (b) Virtual *C*.

and steady-state conditions, confirming its advantages over alternative methods.

Furthermore, to verify the effect of active damping parameters. Similarly, under the load condition where the resistive load is maintained at 20 kW and the CPL power is 60 kW. Fig. 25 shows the waveforms of the system when different C_{ad} is applied. As C_{ad} increases, the system transitions from unstable oscillation to oscillation at a lower frequency, which is caused by the pole in the right half plane of the closed-loop control. Conversely, as C_{ad} decreases, the amplitude of the system oscillation is damped, but the system remains unstable. These results are consistent with the theoretical analysis in Section III-E.

Using the stabilization region provided in Fig. 18, Fig. 26 presents the waveforms of each observation point as the system maintains a 20 kW resistive load and gradually increases the CPL power. The results demonstrate that selecting values within this region ensures stable system operation across all operating conditions.

Fig. 27 further illustrates the impact of different C_{ad} values on the system's transient response within the stabilization region. The results indicate that increasing C_{ad} reduces the voltage regulation time during sudden addition or removal of CPL conditions, thereby improving the transient response to some extent.

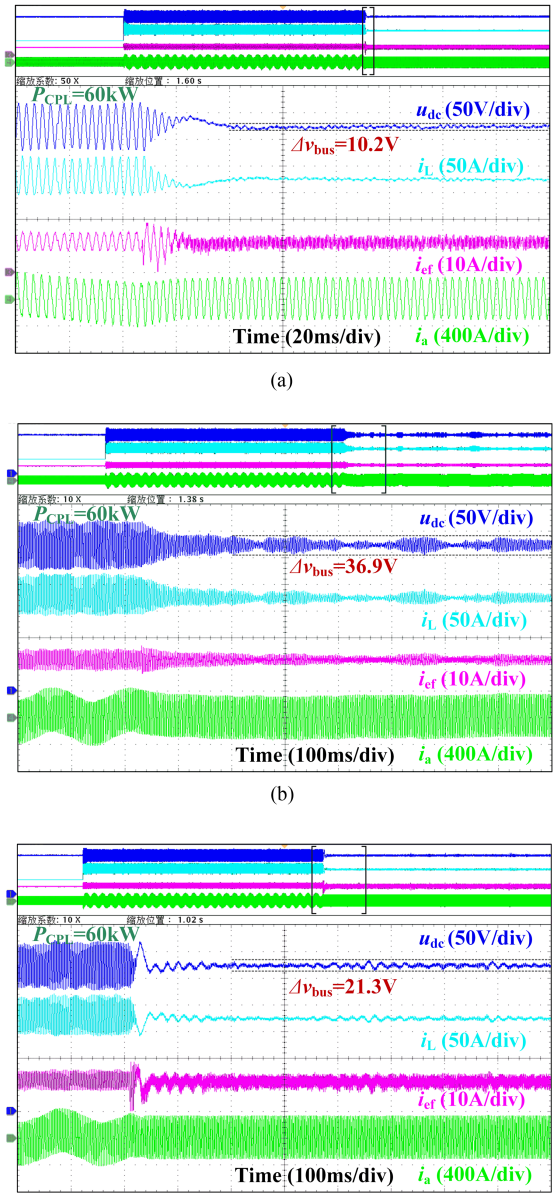

Fig. 25. Experimental results under different C_{ad}. (a) Zoomed view of the C_{ad} value 1.0 p.u. (b) Zoomed view of the C_{ad} value 0.5 p.u. (c) Zoomed view of C_{ad} value 2.5 p.u.

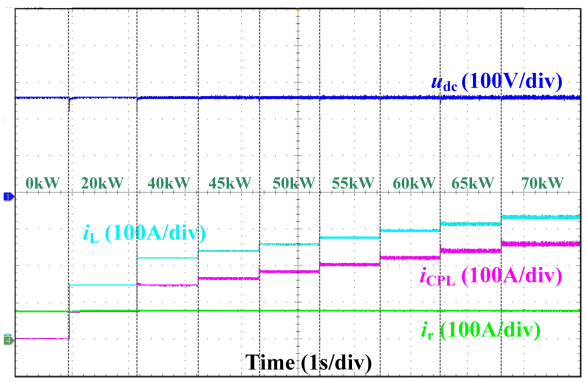

Fig. 26. Experimental results after adding the virtual *RC*-based active damping control strategy. (C_{ad} value 1.0 p.u.).

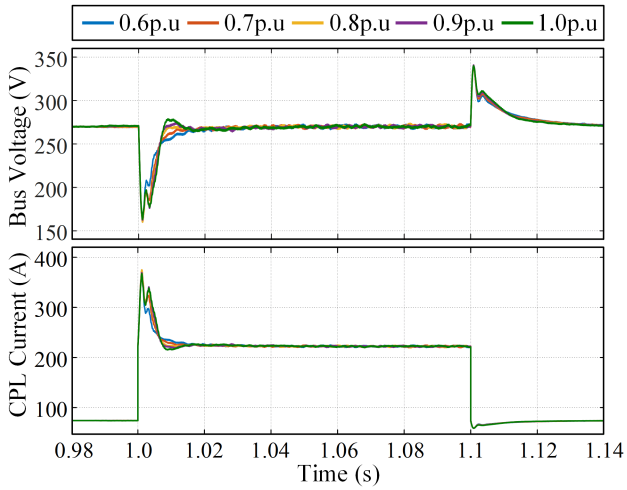

Fig. 27. Experimental transient results for different C_{ad} values.

V. Conclusion

In this article, an active damping control strategy is investigated to enhance the stability of the WRSG-based HVDC system for MEA. A detailed derivation of the small-signal impedance model of the WRSG under double-loop control is presented, along with design principles for control parameters. The impact of CPL and control bandwidth on system stability is analyzed, and the system's instability boundaries as well as the limitations of the conventional PI control are discussed. Based on the active damping method, the effects of the damping position and configuration on stability enhancement are analyzed, and an active damping control strategy based on the virtual resistance and capacitance series is proposed. The relationship between the output current and the field current is derived and extended to full-load conditions, accounting for the strong nonlinearity of the WRSG. The stability boundaries of the system are summarized, and parameter selection methods are provided. An experimental platform is developed to verify the accuracy of the derived impedance model and the effectiveness of the proposed active damping control strategy.

The proposed virtual *RC*-based active damping control strategy can enhance the stability of WRSG-based HVDC power supply system operating under CPL conditions. Furthermore, both the strategy and its parameter selection methodology are applicable to other WRSGs.

Appendix

Based on (7), the field current consists of a dc part related to v_{f} and an ac part related to the d-axis current i_{d}. Since the voltage is contributed only by the dc part, $G_{\mathrm{ef}}(s)$ can be rewritten as

$$G_{\mathrm{ef}}(s) = 1/(sL_{\mathrm{ef}} + R_{\mathrm{ef}}). \tag{A1}$$

Based on (12) and (A1), $G_{\mathrm{iopen}}(s)$ can be further written as

$$G_{\mathrm{iopen}}(s) = \frac{\sqrt{3}\omega_{\mathrm{eP}}\phi_m k_{\mathrm{pi}}(s + k_{\mathrm{ii}}/k_{\mathrm{pi}})}{L_{\mathrm{ef}}s(s + R_{\mathrm{ef}}/L_{\mathrm{ef}})}. \tag{A2}$$

The current loop bandwidth ω_{ci} and can be expressed as

$$\omega_{\mathrm{ci}} = \sqrt{3}\omega_{\mathrm{eP}}\phi_m k_{\mathrm{pi}} \Big/ L_{\mathrm{ef}}. \tag{A3}$$

The inner loop component of the field current can be replaced by (13), and the open-loop transfer function of the voltage loop can, thus, be expressed as

$$G_{\mathrm{vopen}}(s) = k_{\mathrm{ef}} G_{\mathrm{cv}}(s) G_{\mathrm{iclose}}(s) K_{\mathrm{v}} G_{\mathrm{if-vdq}}(s) \tag{A4}$$

where $G_{\mathrm{cv}}(s)$ denotes the transfer function of the voltage PI regulator and $G_{\mathrm{if\text{-}vdq}}(s)$ represents the transfer function from the field current to the *dq*-axis voltage.

Based on (13) and (A4), the closed-loop transfer function $G_{\mathrm{vclose}}(s)$ can be further written as

$$\begin{aligned} G_{\mathrm{v\_close}}(s) &= \frac{G_{\mathrm{vopen}}(s)}{1+G_{\mathrm{vopen}}(s)} \\ &= \frac{\begin{array}{c} k_{\mathrm{ef}}\omega_{\mathrm{ci}}k_{\mathrm{v}}L_{\mathrm{md}}[k_{\mathrm{pv}}\sin\delta s^2 + s(k_{\mathrm{iv}}\sin\delta + \\ k_{\mathrm{pv}}\cos\delta\omega_{\mathrm{e}}) + k_{\mathrm{iv}}\cos\delta\omega_{\mathrm{e}}] \end{array}}{\begin{array}{l} (1+k_{\mathrm{ef}}\omega_{\mathrm{ci}}k_{\mathrm{v}}L_{\mathrm{md}}k_{\mathrm{pv}}\sin\delta)s^2 + s[k_{\mathrm{ef}}\omega_{\mathrm{ci}}k_{\mathrm{v}}L_{\mathrm{md}}(k_{\mathrm{iv}}\sin\delta + \\ k_{\mathrm{pv}}\cos\delta\omega_{\mathrm{e}}) + \omega_{\mathrm{ci}}] + k_{\mathrm{ef}}\omega_{\mathrm{ci}}k_{\mathrm{v}}L_{\mathrm{md}}k_{\mathrm{iv}}\cos\delta\omega_{\mathrm{e}} \end{array}}. \end{aligned} \tag{A5}$$

REFERENCES

[1] P. Wheeler and S. Bozhko, "The more electric aircraft: Technology and challenges," *IEEE Electrific. Mag.*, vol. 2, no. 4, pp. 6–12, Dec. 2014.

[2] B. Sarlioglu and C. T. Morris, "More electric aircraft: Review, challenges, and opportunities for commercial transport aircraft," *IEEE Trans. Transp. Electrific.*, vol. 1, no. 1, pp. 54–64, Jun. 2015.

[3] G. Buticchi, P. Wheeler, and D. Boroyevich, "The more-electric aircraft and beyond," *Proc. IEEE*, vol. 111, no. 4, pp. 356–370, Apr. 2023.

[4] X. Roboam, B. Sareni, and A. D. Andrade, "More electricity in the air: Toward optimized electrical networks embedded in more-electrical aircraft," *IEEE Ind. Electron. Mag.*, vol. 6, no. 4, pp. 6–17, Dec. 2012.

[5] V. Madonna, P. Giangrande, and M. Galea, "Electrical power generation in aircraft: Review, challenges, and opportunities," *IEEE Trans. Transp. Electrific.*, vol. 4, no. 3, pp. 646–659, Sep. 2018.

[6] G. Buticchi, S. Bozhko, M. Liserre, P. Wheeler, and K. Al-Haddad, "On-board microgrids for the more electric aircraft—Technology review," *IEEE Trans. Ind. Electron.*, vol. 66, no. 7, pp. 5588–5599, Jul. 2019.

[7] J. Chen, C. Wang, and J. Chen, "Investigation on the selection of electric power system architecture for future more electric aircraft," *IEEE Trans. Transp. Electrific.*, vol. 4, no. 2, pp. 563–576, Jun. 2018.

[8] W. Cao, B. C. Mecrow, G. J. Atkinson, J. W. Bennett, and D. J. Atkinson, "Overview of electric motor technologies used for more electric aircraft (MEA)," *IEEE Trans. Ind. Electron.*, vol. 59, no. 9, pp. 3523–3531, Sep. 2012.

[9] E. Sayed et al., "Review of electric machines in more-/hybrid-/turbo-electric aircraft," *IEEE Trans. Transp. Electrific.*, vol. 7, no. 4, pp. 2976–3005, Dec. 2021.

[10] K.-N. Areerak, S. V. Bozhko, G. M. Asher, L. De Lillo, and D. W. P. Thomas, "Stability study for a hybrid AC-DC more-electric aircraft power system," *IEEE Trans. Aerosp. Electron. Syst.*, vol. 48, no. 1, pp. 329–347, Jan. 2012.

[11] F. Gao and S. Bozhko, "Modeling and impedance analysis of a single DC bus-based multiple-source multiple-load electrical power system," *IEEE Trans. Transp. Electrific.*, vol. 2, no. 3, pp. 335–346, Sep. 2016.

[12] C. Zhang, X. Ruan, Y. He, and S. Wang, "Modular modeling and bus-port impedance analysis of DC three-stage generator for more electric aircraft," *IEEE Trans. Power Electron.*, vol. 38, no. 12, pp. 15579–15588, Dec. 2023.

[13] J. Yang et al., "Modeling and stability enhancement of a permanent magnet synchronous generator based DC system for more electric aircraft," *IEEE Trans. Ind. Electron.*, vol. 69, no. 3, pp. 2511–2520, Mar. 2022.

[14] F. Gao et al., "Comparative stability analysis of droop control approaches in voltage-source-converter-based DC microgrids," *IEEE Trans. Power Electron.*, vol. 32, no. 3, pp. 2395–2415, Mar. 2017.

[15] F. Gao, S. Bozhko, A. Costabeber, G. Asher, and P. Wheeler, "Control design and voltage stability analysis of a droop-controlled electrical power system for more electric aircraft," *IEEE Trans. Ind. Electron.*, vol. 64, no. 12, pp. 9271–9281, Dec. 2017.

[16] B. Zhang, F. Gao, Y. Zhang, D. Liu, and H. Tang, "An AC-DC coupled droop control strategy for VSC-based DC microgrids," *IEEE Trans. Ind. Electron.*, vol. 37, no. 6, pp. 6568–6584, Jun. 2022.

[17] R. Kumar and C. N. Bhende, "A virtual adaptive RC damper control method to suppress voltage oscillation in DC microgrid," *Int. J. Elect. Power Energy Syst.*, vol. 146, Mar. 2023, Art. no. 108795.

[18] O. Lorzadeh, I. Lorzadeh, M. N. Soltani, and A. Hajizadeh, "Source-side virtual RC damper-based stabilization technique for cascaded systems in DC microgrids," *IEEE Trans. Energy Convers.*, vol. 36, no. 3, pp. 1883–1895, Sep. 2021.

[19] Q. Xu, N. Vafamand, L. Chen, T. Dragičević, L. Xie, and F. Blaabjerg, "Review on advanced control technologies for bidirectional DC/DC converters in DC microgrids," *IEEE J. Emerg. Sel. Topics Power Electron.*, vol. 9, no. 2, pp. 1205–1221, Apr. 2021.

[20] M. Wu and D. D.-C. Lu, "A novel stabilization method of LC input filter with constant power loads without load performance compromise in DC microgrids," *IEEE Trans. Ind. Electron.*, vol. 62, no. 7, pp. 4552–4562, Jul. 2015.

[21] M. N. Hussain, R. Mishra, and V. Agarwal, "A frequency-dependent virtual impedance for voltage-regulating converters feeding constant power loads in a DC microgrid," *IEEE Trans. Ind. Appl.*, vol. 54, no. 6, pp. 5630–5639, Nov./Dec. 2018.

[22] J. Liao, C. Guo, Y. Huang, G. Qiu, N. Zhou, and Q. Wang, "Active damping control of cascaded DC converter in DC microgrids based on optimized parallel virtual resistance," *IEEE J. Emerg. Sel. Topics Ind. Electron.*, vol. 4, no. 2, pp. 560–570, Apr. 2023.

[23] J. Huang, Z. Zhang, and J. Han, "Stability analysis of permanent magnet generator system with load current compensating method," *IEEE Trans. Smart Grid*, vol. 13, no. 1, pp. 58–70, Jan. 2022.

[24] Z. Qu, Z. Zhang, J. Li, and H. Shi, "Investigation of nonlinear PI multi-loop control strategy for aircraft HVDC generator system with wound rotor synchronous machine," *CES Trans. Elect. Mach. Syst.*, vol. 7, no. 1, pp. 92–99, Mar. 2023.

[25] X. Fan, Z. Zhang, J. Li, Y. Xu, and J. Han, "Fuzzy PI multi-loop control of wound rotor synchronous machine for aircraft variable frequency AC generation system," in *Proc. 22nd Int. Conf. Elect. Mach. Syst.*, Aug. 2019, pp. 1–6.

[26] H. Shi and Z. Zhang, "Dual internal model control with improved load current feedback for enhanced dynamic performance in aircraft high-voltage direct current brushless generator," *IET Elect. Power Appl.*, vol. 18, no. 10, pp. 1174–1186, Jun. 2024.

[27] R. Patel, F. Hafiz, A. Swain, and A. Ukil, "Nonlinear excitation control of diesel generator: A command filter backstepping approach," *IEEE Trans. Ind. Inform.*, vol. 17, no. 7, pp. 4809–4817, Jul. 2021.

[28] J. Wang, S. Yang, L. Gu, and L. Wang, "Research on voltage regulation technology of aircraft 270V brushless DC power generation system based on H-infinity robust control," in *Proc. 8th Asia Conf. Power Elect. Eng.*, Apr. 2023, pp. 2413–2418.

[29] H. Shi, Z. Zhang, J. Han, and J. Li, "Dynamic performance improvement of wound rotor synchronous starter/generator system based on PWM rectifier," *IEEE Trans. Transp. Electrific.*, vol. 9, no. 3, pp. 4639–4649, Sep. 2023.

[30] I. Jadric, D. Borojevic, and M. Jadric, "Modeling and control of a synchronous generator with an active DC load," *IEEE Trans. Power Electron.*, vol. 15, no. 2, pp. 303–311, Mar. 2000.

[31] J. Li, Z. Zhang, J. Lu, Y. Liu, and Z. Chen, "Design and characterization of a single-phase main exciter for aircraft wound-rotor synchronous starter–generator," *IEEE Trans. Magn.*, vol. 54, no. 11, Nov. 2018, Art. no. 8206805.

[32] J. Li, Z. Zhang, J. Lu, H. Li, and Z. Chen, "Investigation and analysis of a new shaded-pole main exciter for aircraft starter–generator," *IEEE Trans. Magn.*, vol. 53, no. 11, Nov. 2017, Art. no. 8209604.

[33] B. He, W. Chen, X. Li, L. Shu, and X. Ruan, "A power adaptive impedance reshaping strategy for cascaded DC system with buck-type constant power load," *IEEE Trans. Power Electron.*, vol. 37, no. 8, pp. 8909–8920, Aug. 2022.

Yiming Yao received the B.S. degree in electrical engineering in 2019 from the Nanjing University of Aeronautics and Astronautics, Nanjing, China, where he is currently working toward the Ph.D. degree in electrical engineering.

His main research interests include stability control of electric power system for more electric aircraft.

Zhuoran Zhang (Senior Member, IEEE) received the B.S. degree in measurement engineering and the M.S. and Ph.D. degrees in electrical engineering from the Nanjing University of Aeronautics and Astronautics (NUAA), Nanjing, China, in 2000, 2003, and 2009, respectively.

Since 2003, he has been a member of the faculty at the Department of Electrical Engineering, NUAA, where he is currently a Full Professor. He is also the Dean of the College of Civil Aviation, NUAA. From Feburary 2012 to June 2013, he was a visiting professor in Wisconsin Electric Machines and Power Electronics Consortium (WEMPEC), University of Wisconsin-Madison, Madison, WI, USA.

His research interests include electrical machines and drives with emphasis on permanent magnet machines, hybrid excitation electric machines, and doubly salient electric machines for aircraft power, electric vehicles, and renewable energy generation. He has authored or coauthored over 230 technical papers and two books and is the holder of 61 issued patents in these areas. He was the recipient of the Best Paper Awards from IEEE VPPC 2013, IEEE ICEMS 2023 and ICEM 2024.

Yankun Wang (Graduate Student Member, IEEE) received the B.S. degree in measurement engineering from the North China Electric Power University, Beijing China, in 2021 and the M.Sc. degree in electronic and electrical engineering from Durham University, Durham, U.K., in 2023. He is currently working toward the Ph.D. degree in electrical engineering with Nanjing University of Aeronautics and Astronautics, Nanjing, China.

His research interests include integrated starter/generator system and high-performance electrical machine control algorithms for more electric aircraft.

Yiwei Yang received the B.S. and M.S. degrees in electrical engineering in 2010 and 2013, respectively, from the Nanjing University of Aeronautics and Astronautics, Nanjing, China, where he is currently working toward the Ph.D. degree in electrical engineering.

His research interests include the design of electric power system architectures and control of starter generators for more electric aircraft.

Heng Shi received the B.S. degree in communication engineering from Zhengzhou University, Zhengzhou, China, in 2013, the M.S. degree in electrical engineering from Lanzhou University of Technology, Lanzhou, China, in 2017, and the Ph.D. degree in electrical engineering from the Nanjing University of Aeronautics, Nanjing, China, in 2024.

His research interests include control of brushless synchronous starter/generator and electrical power generation system for more electric aircraft.

Jincai Li received the B.S. degree from the Henan University of Urban Construction, Pingdingshan, China, in 2012, the M.S. degree from Shanghai Dianji University, Shanghai, China, in 2015, and the Ph.D. degree from the Nanjing University of Aeronautics, Nanjing, China, in 2020, all in electrical engineering.

He is currently a Post-Doctoral Researcher with NUAA. His research interests include the design and control of brushless synchronous starter/generator and electrical power generation systems for more electric aircraft.